



Cite this: *Soft Matter*, 2020,  
16, 3325

# Small-scale demixing in confluent biological tissues†

Preeti Sahu, <sup>a\*</sup> Daniel M. Sussman, <sup>ab</sup> Matthias Rübsam, <sup>c</sup> Aaron F. Mertz, <sup>d</sup>  
 Valerie Horsley, <sup>e</sup> Eric R. Dufresne, <sup>dfg</sup> Carien M. Niessen, <sup>c</sup>  
 M. Cristina Marchetti, <sup>h</sup> M. Lisa Manning <sup>a</sup> and J. M. Schwarz <sup>\*ai</sup>

Surface tension governed by differential adhesion can drive fluid particle mixtures to sort into separate regions, *i.e.*, demix. Does the same phenomenon occur in confluent biological tissues? We begin to answer this question for epithelial monolayers with a combination of theory *via* a vertex model and experiments on keratinocyte monolayers. Vertex models are distinct from particle models in that the interactions between the cells are shape-based, as opposed to distance-dependent. We investigate whether a disparity in cell shape or size alone is sufficient to drive demixing in bidisperse vertex model fluid mixtures. Surprisingly, we observe that both types of bidisperse systems robustly mix on large lengthscales. On the other hand, shape disparity generates slight demixing over a few cell diameters, a phenomenon we term micro-demixing. This result can be understood by examining the differential energy barriers for neighbor exchanges (T1 transitions). Experiments with mixtures of wild-type and E-cadherin-deficient keratinocytes on a substrate are consistent with the predicted phenomenon of micro-demixing, which biology may exploit to create subtle patterning. The robustness of mixing at large scales, however, suggests that despite some differences in cell shape and size, progenitor cells can readily mix throughout a developing tissue until acquiring means of recognizing cells of different types.

Received 29th May 2019,  
Accepted 22nd February 2020

DOI: 10.1039/c9sm01084j

[rsc.li/soft-matter-journal](http://rsc.li/soft-matter-journal)

Liquid–liquid phase separation, *i.e.*, demixing, drives patterning. In materials science, demixing between two liquids is typically driven by the energetics of interfacial tension overcoming entropy-driven mixing.<sup>1</sup> By cooling a material, one can tune between a mixed state at high temperature and a demixed state at low temperature. Depending on the material and quench rate, this transition can occur continuously *via* spinodal decomposition or discontinuously *via* nucleation.<sup>2,3</sup> In order to distinguish between mechanisms it is often useful to analyze the lengthscales of

emergent patterns: nucleation and spinodal decomposition give rise to characteristic lengthscales that then coarsen, while in the absence of interfacial tension fluids will mix down to the scale of single molecules. These and related demixing phenomena have been studied numerically using multicomponent Lennard-Jones mixtures in which particles have a fixed shape and an interaction potential that depends on the distance between. The potential also energetically distinguishes between particles of different types to model interfacial tension.<sup>4</sup>

In biology, demixing at the subcellular scale can lead to compartmentalization within cells,<sup>5</sup> while in a developing organism, demixing can lead to compartmentalization among cells of different type, otherwise known as cell sorting. In fact, interfacial tension-driven demixing has long been invoked to explain cellular patterning. The first among such ideas is the Differential Adhesion Hypothesis (DAH), proposed by Steinberg in 1963,<sup>6</sup> to explain patterns in the spatial sorting of progenitor cells, such as ectoderm and mesoderm, during embryonic development. The DAH postulates that tissues behave like immiscible liquids composed of motile cells that rearrange in order to minimize their interfacial tension caused by differences in cell–cell adhesion. Building on the DAH, Harris,<sup>7</sup> and later Brodland,<sup>8</sup> have highlighted the importance of other contributors to interfacial tension, including regulation of the acto-myosin cortex. There is an emerging consensus<sup>9–13</sup> that

<sup>a</sup> Department of Physics and BioInspired Syracuse, Institute for Material and Living Systems, Syracuse University, Syracuse, NY 13244, USA. E-mail: [prsahu@syr.edu](mailto:prsahu@syr.edu), [jschwarz@physics.syr.edu](mailto:jschwarz@physics.syr.edu)

<sup>b</sup> Department of Physics, Emory University, Atlanta, GA, 30322, USA

<sup>c</sup> Department of Dermatology, CECAD Cologne, Center for Molecular Medicine, University of Cologne, Cologne, Germany

<sup>d</sup> Department of Physics, Yale University, New Haven, CT 06520, USA

<sup>e</sup> Department of Molecular, Cellular and Developmental Biology, Yale University, New Haven, CT 06520, USA

<sup>f</sup> Departments of Mechanical Engineering and Materials Science, Chemical and Environmental Engineering, and Cell Biology, Yale University, New Haven, CT, 06520, USA

<sup>g</sup> Department of Materials, ETH Zürich, 8093 Zürich, Switzerland

<sup>h</sup> Department of Physics, University of California at Santa Barbara, Santa Barbara, CA 93106, USA

<sup>i</sup> Indian Creek Farm, Ithaca, NY 14850, USA

† Electronic supplementary information (ESI) available. See DOI: 10.1039/c9sm01084j

adhesive molecules help to regulate cortical acto-myosin, which can strongly impact cell sorting. However, it remains controversial whether differential adhesion or differential cortical tension alone is sufficient to generate the level of cell sorting and compartmentalization observed in embryos and cell culture systems.<sup>14–20</sup> Several experiments have suggested that additional processes such as specialized cell–cell signaling<sup>16</sup> or cellular jamming<sup>17</sup> enhance or disrupt sorting in living tissues.

One major difference between immiscible liquids composed of cells and immiscible liquids composed of soft spheres is that in the latter case, the particles have a distance-dependent interaction, while in epithelial layers and even some 3D tissues, the cells are confluent – they can change their shape to completely fill space—and so their interaction is shape-based. To reflect this property, confluent tissues have been studied theoretically and computationally using vertex or Voronoi models,<sup>21–24</sup> where cells are constructed from tessellations of space with no gaps between cells. As active fluctuations drive cellular rearrangements, cells must deform so that no gaps open up between them. This suggests cells are subject to strong geometrical and topological constraints. For example, in flat 2D tilings with three-fold coordinated vertices, the average number of neighbors must be precisely six. This constraint leads one to predict that a rigidity transition should occur when neighbor exchange between six-sided cells cost zero energy, *i.e.* when cells can form regular pentagons at zero cost.<sup>25,26</sup> This prediction has since been realized in experiments<sup>27</sup> and is distinct from rigidity transitions in particulate systems.<sup>28,29</sup>

Does such an interaction potential with non-trivial geometrical and topological constraints affect the fundamental definition of surface tension? Work on bidisperse foams modeled as ordered vertex models demonstrate that, in equilibrium, demixed cells of two different areas have a lower energy than a mixed system and so demixed states are energetically preferred.<sup>30</sup> However, disperse-in-area foams under large shear strain will mix.<sup>31</sup> If we think of the shear strain as a temperature-like variable, then these findings are similar to particulate systems.

On the other hand, recent work by some of us demonstrates that so-called heterotypic contacts in vertex models can drastically affect the notion of interfacial tension.<sup>32</sup> Heterotypic contacts, where cells recognize neighbors of a different cell type, can be modeled in two-dimensional vertex models with a higher or lower line tension along interfaces between cells of different types, or heterotypic line tension. Such a rule results in very sharp, yet deformable, interfaces<sup>32</sup> where surface tension measured by macroscopic deformation of an overall droplet shape gives a value in line with equilibrium expectations, yet, surface tension measured from interfacial fluctuations is at least an order of magnitude larger. This discrepancy is due to discontinuous pinning forces generated during topological rearrangements between cells of different types. That is, it is a consequence of the shape-based nature of the interactions.

Here, we explore the possibility of interfacial-tension-driven demixing in the absence of explicit heterotypic tension in both modeling and in experiments. From the modeling side, we consider a two-dimensional vertex model with two different cell types.

Particulate mixtures can demix when a miscibility parameter, the ratio of the strength of the distance-dependent interaction between dissimilar particles as compared to similar particles, becomes less than one. Since in vertex models the interaction is shape-based, it is natural to ask if binary vertex model fluids consisting of mixtures of cells with different preferred cell shapes and/or sizes, accounting for differential adhesion, cortical tension or volume, demix even in the absence of specialized heterotypic interactions. In other words, is there an emergent effective interfacial tension between two cell types that is sufficient enough to sort cells? Should the answer be yes, then one can imagine that the sorting of progenitor cells occurs very early on in the development process before robust heterotypic interfacial tensions are established. Should the answer be no, then cells must establish heterotypic interactions before sorting can occur, suggesting a more important mechanical role for cell recognition receptors than previously thought. The topological nature of the discontinuous pinning forces stabilizing interfaces in vertex model fluid mixtures tells us that once such recognition is in place, a finite active force is required to overcome the discontinuity.<sup>32</sup> Interestingly, a recent study with both *in vitro* experiments and cellular Potts model simulations suggests that a large heterotypic line tension is required for cell sorting,<sup>33</sup> although the mechanism was left unresolved.

In searching for whether or not large-scale interfacial tensions and, therefore, cell demixing are emergent/collective properties of such binary vertex model fluid mixtures, we do not observe large-scale demixing. However, we do observe small-scale demixing in mixtures with differential adhesion, which is not thermodynamic in origin and which we term micro-demixing. We find that this behavior arises from dynamical trapping due to energy barriers to neighbor exchanges (T1 transitions) that depend on configuration of the type of cell. We then ask if the predicted phenomenon of micro-demixing can be realized in cellular systems.

To begin to answer this question, we experimentally study monolayers of mixtures of wild-type primary keratinocytes, denoted as Ctr cells, and primary keratinocytes in which the E-cadherin has been knocked down, denoted as E-cad<sup>−/−</sup> cells. Cadherins, such as E-cadherin and P-cadherin, are crucial components of adherens junctions (AJs) that couple intercellular adhesion to the cytoskeleton *via*  $\alpha$ - and  $\beta$ -catenin,<sup>34</sup> the former of which can interact directly with actin and other actin binding proteins. It has been even more recently established that E-cadherin plays a central role in the mechanical circuitry coordinating adhesion, contractile forces and biochemical signaling to drive polarized organization of tension observed in stratified epidermal layers.<sup>35</sup> Given the central role of E-cadherin, E-cad<sup>−/−</sup> keratinocytes affect the mechanical circuitry *via*, for example, decreased adhesion site lengths.<sup>35</sup> Since the wild-type keratinocytes contain both P- and E-cadherin, two-dimensional mixtures of the wild-type keratinocytes with E-cad<sup>−/−</sup> keratinocytes are ideal for testing whether or not differential adhesion leads to large-scale demixing or not, even in the absence of heterotypic tensions. In addition to the lack of large-scale demixing in the experiments, we also find evidence for small-scale demixing as predicted in our two-dimensional vertex

model, further bolstering the use of this class of models as a predictor of tissue rheology.

## Computational model

Cells are biomechanical (and biochemical) constructs that are not in equilibrium, *i.e.* they are driven by active forces. Given our question of mixing, we study a confluent monolayer of cells of different types. The biomechanics of the  $j$ th cell of type  $\beta$  is given by the energy functional:

$$E_{j,\beta} = K_a(A_{j,\beta} - A_{0,\beta})^2 + K_p(P_{j,\beta} - P_{0,\beta})^2, \quad (1)$$

where  $A_{j,\beta}$  denotes the  $j$ th cell area of type  $\beta$  and the  $j$ th cell perimeter of type  $\beta$  is denoted by  $P_{j,\beta}$ . Given the quadratic penalty from deviating for a cell's preferred area and perimeter,  $K_a$  and  $K_p$  are area and perimeter stiffnesses, respectively, and both are independent of cell type. Physically, the area term represents the bulk elasticity of the cell, while the perimeter term represents the contractility of the acto-myosin cortex with  $P_{0,\beta}$  denoting a competition between cortical tension and cell-cell adhesion. The total energy of the tissue is then defined as  $E = \sum_{j,\beta} E_{j,\beta}$ . An important parameter in these models is the dimensionless shape index  $s_{0,\beta} = P_{0,\beta} / \sqrt{A_{0,\beta}}$ . A regular hexagon has a dimensionless shape index of  $s_0 \approx 3.72$ , for example.

To study binary mixtures, we fix  $\beta = 1, 2$  and allow the cell types to have different parameters,  $A_{0,\beta}$  and  $s_{0,\beta}$  (see Fig. 1a). What is the biological implication of two different shape indices, for example? Consider two cell-types with the exact same area. The cell type that prefers to have a higher shape index, can do so by increasing the density of adhesion molecules, for example. Therefore, mixing these two differently adhering cell-types corresponds to studying mixing in cell-types with two different shapes. In reality, these adhesion receptors also affect the cell shape by signaling to either up-regulate or down-regulate contractility. In the vertex model energy functional that we use,

we have packaged both adhesion and contractility into the preferred shape index. Though more detailed models are possible, we find that our minimal model does indeed tell us something about how cells behave as indicated by the experiments presented below. We will focus on cases of 50 : 50 mixtures where there is an equal number of each cell type, with either preferred shape disparity or preferred area disparity. Unless otherwise specified, the two components are uniformly distributed in the initial state. We set  $K_p$  to unity for all systems.

We study the above energy functional from an energy minimization perspective as well as from a dynamical perspective in which the cells migrate within the monolayer. As for the latter, there is still much debate about how to model the motility of cells. We have chosen to model the motility of a cell by imposing a random active force on each vertex, *i.e.* each vertex undergoes over-damped Brownian motion at a fixed effective temperature  $T$  with a conservative force contribution from the above energy functional and a second force contribution from a Brownian force. While there are other possible dynamical rules, we have found that, for example, the properties of an interface between two cell types with heterotypic line tension between them is rather robust to the specifics of the dynamical rule.<sup>32</sup> The equation of motion for each vertex is then iterated until the cells can adequately explore the entire system such that the system approaches a steady state, at least for most parameters we study. As the cells move, they may rearrange and come into contact with new cells. Such rearrangements are known as T1 transitions. To implement a T1 transition, an edge shared between two cells undergoes a  $\pi/2$  rotation once the length of this edge is below some threshold length. The rotated edge then lengthens and allows for two different cells to now share an edge. As for the energy minimization approach, in addition to comparing the minimum energy configurations of both demixed and mixed states, we will also compute the energy barriers associated with T1 transitions by constraining the length of a particular edge in the system such that a T1

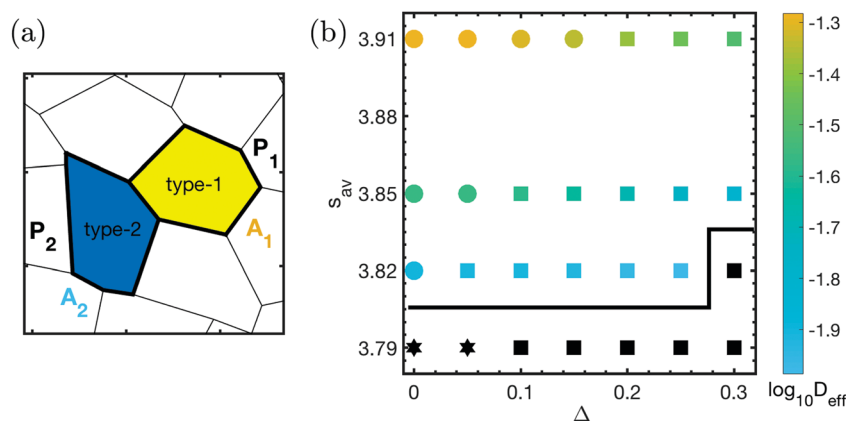


**Fig. 1** Vertex model binary mixtures. (a) Schematic of vertex-based modeling of a tissue: a typical tessellation with two different types of cells highlighted. The energy depends only on a cell's perimeter ( $P_j$ ) and area ( $A_j$ ). (b) A heat map of  $\log_{10} D_{\text{eff}}$  as a function of  $\Delta$  on the x-axis and  $s_{\text{av}}$  on the y-axis. The phase points with: fluid–fluid ( $s_{0,1}, s_{0,2} > 3.81$ ), solid–fluid ( $s_{0,1} < 3.81$ ) and solid–solid ( $s_{0,1}, s_{0,2} < 3.81$ ) components are denoted by circular, square and star-shaped markers, respectively. Black-filled markers, demarcated by a solid black line, denote mixtures with a  $D_{\text{eff}}$  less than that of the chosen cutoff of 0.01. Region above this line denotes fluid-like behaviour on average.

transition occurs while allowing the remaining degrees of freedom in the system to relax. See the Methods section for more details.

We are also interested in comparing the behavior of these bidisperse systems to ones with an explicit heterotypic line tension (HLT), where cell types 1 and 2 recognize their joint interface as a heterotypic interface and, therefore, alter the line tension at that interface. Such interactions are common in cellular Potts models<sup>33,36</sup> and have also been studied in vertex and Voronoi models.<sup>24,32</sup> In this case, we add an extra term to the cell energy to arrive at:

$$E_{\text{HLT}} = \sum_{j,\beta} K_a (A_{j,\beta} - A_{0,\beta})^2 + K_p (P_{j,\beta} - P_{0,\beta})^2 + \gamma \sum_{\langle i,j \rangle} (1 - \delta_{\alpha\beta}) l_{ij}. \quad (2)$$

The latter sum is over all edges,  $l_{ij}$ , between cells  $i$  and  $j$  with  $\delta_{\alpha\beta}$  representing a Kronecker delta such that there is additional line tension only between cells of two different types  $\alpha$  and  $\beta$ . For simplicity, we assume that the additional tension,  $\gamma$ , is the same for all heterotypic edges.

## Computational results

### Stability and fluidity of shape bidisperse mixtures

To single out the effect of shape dispersity, we first vary the preferred shapes under the constraint that the preferred/target area is the same across cell types,  $A_{0,1} = A_{0,2} = 1$ .

Previous work on the vertex model has identified a regime in parameter space dominated by a coarsening instability,<sup>22,23</sup> where some cells shrink in size and others grow. We expect that heterogeneous  $s_0$  values might amplify this instability, as heterogeneity amplifies differences between the cells. To prevent area dispersity from affecting the results in these mixtures, we choose  $K_a = 100$ , which is sufficient to reduce fluctuations in area  $A$  from target area  $A_0$  to a standard deviation of less than 1%, preventing the onset of the coarsening instability. Moreover, Fig. S1 (ESI†) shows that increased area stiffness does not significantly impact the fluidity of homogeneous tissues, as measured by the effective diffusivity (eqn (6)–(8)), denoted as  $D_{\text{eff}}$ , which is the ratio of the diffusion constant in the presence of interactions to that in the absence of interactions. The onset of a finite effective diffusivity as a function of the shape index remains near  $s_0 \approx 3.81$  with increasing  $K_a$ .

Next, we investigate how shape disparity affects the fluidity of the tissue. We find that the most effective way to represent the phase space of the two-component system with two shape indices  $s_{0,1}, s_{0,2}$  is by the average value of the shape index,  $s_{\text{av}} = (s_{0,1} + s_{0,2})/2$ , and the shape disparity, which is the difference between the two values,  $\Delta = s_{0,2} - s_{0,1}$  with  $s_{0,2} > s_{0,1}$ . Fig. 1b is a heat map of the effective diffusivity of binary mixtures as a function of  $s_{\text{av}}$  and  $\Delta$ . We see that there is a boundary between fluid-like and solid-like, demarcated by the thick solid line, as determined by the  $D_{\text{eff}}$  threshold. Interestingly, for  $\Delta = 0.3$ , this boundary does not match up with the fluid–solid

boundary for the monodisperse case for the Brownian limit of a self-propelled Voronoi model at a similar temperature, which is near  $s_0 = 3.81$ .<sup>26</sup> Moreover, the solid–fluid mixtures depicted by squares, have a fluid-like diffusivity above the boundary line. This indicates that the fluid-like species in the mixture are sufficient to fluidize the entire tissue, which is additionally confirmed by analyzing the diffusivities of each component (Fig. S2a, ESI†).

### Binary mixtures with two target shapes

After understanding how  $\Delta$  affects diffusivity in a mixture, let us now understand its role in bulk demixing for a fixed  $s_{\text{av}} = 3.85$ . A snapshot of a typical long-time configuration for such a mixture is shown in Fig. 2a. By eye, it appears that demixing does occur at very small scales, due to some clustering of the cells with larger  $s_0$ . The system maintains this small-scale structure at long times. No large-scale demixing is observed. Hence, we shall refer to this process as micro-demixing. To quantify micro-demixing and highlight its long-time steady state, we study three observables.

The first is the demixing parameter DP, which measures the average environment of each species, quantifying whether it is more likely to be surrounded by similar (homotypic) or dissimilar (heterotypic) cells. Defining  $N_s$  as the number of similar

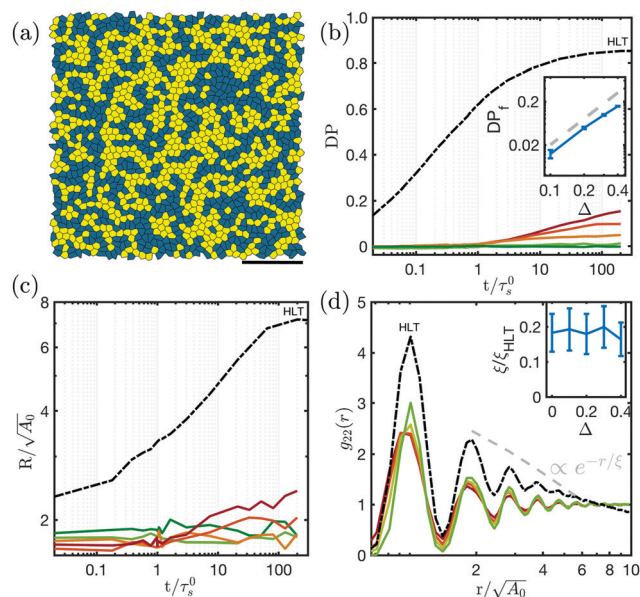


**Fig. 2** Shape bidisperse fluid mixtures. (a) Snapshot of a  $P_{\text{av}} = 3.85$ ,  $\Delta = 0.4$ ,  $N = 1600$  mixture. Scale bar denotes 10 length units. Yellow is used for solid-like cells ( $s_0 = 3.65$ ) and blue for liquid-like ones ( $s_0 = 4.05$ ). (b–d) Various quantifications of demixing in shape bidisperse mixtures (curves colored from green to red in increasing order of shape disparity i.e.  $\Delta = 0.01, 0.1, 0.2, 0.3$  and  $0.4$ ) are compared to a mixture with an extra heterotypic line tension of value 0.1,  $s_0 = 3.97$  (black dashed curve). (b) Demixing parameter versus log(time). The final value ( $DP_f$ ) as a function of  $\Delta$  is shown in the inset. (c) Average cluster radius ( $R$ ) versus time. (d) Pair correlation function of high- $s_0$  cells ( $g_{22}$ ) versus radial distance for  $t = 200\tau_s^0$ . The dashed grey line shows an exponential decay. The inset shows the decay lengthscale ( $\xi$ ) in terms of the maximum possible lengthscale ( $\xi_{\text{HLT}}$ ) with increasing disparity  $\Delta$ . Simulation details provided in Table S1 (ESI†).



neighboring cells and  $N_t$  as the total number of neighboring cells,

$$DP = \langle DP_i \rangle = \left\langle 2 \left( \frac{N_s}{N_t} - \frac{1}{2} \right) \right\rangle, \quad (3)$$

where the brackets denote averaging over all cells in the tessellation. In a completely mixed state,  $DP = 0$ , whereas in a completely sorted mixture,  $DP = 1$ , in the limit of infinite system size.

The demixing parameter as a function of time is shown in Fig. 2b. The value of  $DP$  is initially zero since the two cell types are initially seeded at random, and saturates to a small non-zero value at long times. The final steady state value,  $DP_f$ , increases with increasing shape disparity  $\Delta$ , as shown in the inset to Fig. 2b, and the length of time required to reach the steady state also increases with increasing  $\Delta$  (Fig. S2(b), ESI†). For comparison, the dashed black line in Fig. 2b illustrates the demixing parameter as a function of time for a model with heterotypic line tension. In the HLT case,  $DP$  rises very quickly to a value close to unity as one species rapidly forms a circular droplet, in a manner similar to that expected for conventional liquid–liquid binary mixtures.

We then measure the average cluster radius  $R$  by quantifying the average radius of gyration of the dispersed component. In the case of shape bidisperse mixtures, the more fluid-like (larger  $s_0$ ) component tends to be dispersed. The average cluster radius (Fig. 2c) shows a small growth in time, which appears to saturate at long times, although the data is noisier given the cluster statistics sampling rate. The steady state radius tends to increase with increasing  $\Delta$ . In all cases studied, clusters have an average radius of less than  $2.5 \pm 0.2$ . For comparison, the dashed line shows a system with HLT, which we expect to saturate as a nearly circular droplet of one species embedded inside the other species. For the system size we study, this would correspond to a cluster of radius 8, which is close to the observed steady state value of  $7.2 \pm 0.2$ .

To further quantify the structure of this micro-demixed state, we study the pair correlation function,  $g(r)$ , which describes the normalized probability of finding a cell center a given distance from another cell center. In homogeneous fluids and amorphous solids, this function exhibits short range order with peaks occurring at distances that are integer multiples of the typical spacing between two cells. The envelope of these peaks falls off with distance and eventually approaches unity, highlighting that these materials are disordered over larger lengthscales. In bidisperse mixtures, we compute the correlation between each species  $\beta$  separately, defined by the relative position vectors ( $r^{(\beta)}$ ) between two cells of type  $\beta$ :

$$g_{\beta\beta}(r) = \frac{1}{2\pi r N_{\beta} \rho_0} \sum_i \sum_j \delta(r - r_{ij}^{(\beta)}). \quad (4)$$

For a completely sorted mixture,  $g_{\beta\beta}(r)$  should exhibit an envelope that falls off exponentially, with a length scale  $\xi$  that corresponds to the average cluster radius. In the HLT mixtures, where a single droplet forms, we see such a structure, as shown

by the dashed black line in Fig. 2d. We extract a length scale of  $\xi_{\text{HLT}} = 4.5 \pm 1.2$ , which is very similar to the steady state average cluster radius shown in Fig. 2c. For comparison, we measure  $\xi$  for all shape bidisperse mixtures and compare it to  $\xi_{\text{HLT}}$  by computing  $\xi/\xi_{\text{HLT}}$  (see inset to Fig. 2d). We find this ratio to be quite small, consistent with previous results.

### Binary mixtures with two target areas

After studying the impact of shape disparity in cell sorting, we next study the effect of dispersity in area. The mixture is now comprised of equal numbers of cells with  $A_{0,1} < A_{0,2}$ , where we take  $\sqrt{A_{0,1}}$  as the unit of length. Both types have the same  $s_0$ , or  $s_{0,1} = s_{0,2}$ . We have taken care to ensure that our area bidisperse mixture are also in a fluid region of the phase diagram (Fig. S1b, ESI†) by checking that  $D_{\text{eff}} > 0.01$ . For the results shown here, the shape index is fixed at  $s_0 = 3.85$  to mimic fluid-like cells. We define the ratio of the preferred areas as  $\alpha = A_{0,2}/A_{0,1}$ .

Visual inspection of a snapshot from a simulation of an area bidisperse mixture with high  $\alpha = 2.5$  at long times demonstrates that observing cluster formation by eye is difficult, particularly given the disparity in area fraction between the two cell types (see Fig. 3). The  $DP$  has been measured and is smaller than those found in shape bidisperse mixtures (Fig. 2b). Since the large- $A_0$  cells occupy more than half of the total area, we perform our cluster analysis on cells with  $A_{0,1}$ . As shown in Fig. 3c, the final clusters have an average cluster radius that is typically less than two cell diameters and becomes smaller as  $\alpha$  increases. Similarly, Fig. 3d illustrates that  $g_{ss}(r)$  also shows no sign of bulk demixing, with a structural length scale that is always less than  $0.2 \times \xi_{\text{HLT}}$ , and decreases with decreasing  $\alpha$ , as seen in the inset to Fig. 3d.

### Zero-temperature energy configurations

Our finite-temperature simulations suggest that large-scale sorting is not preferred in these mixtures. To understand this, we study an ensemble of energy minimized states. If the mixed state has a lower energy at zero temperature, then we expect that energetics cannot drive demixing at finite temperature. Therefore, we compare the energy of two initial states of  $N = 400$  cells: a sorted system where all of the cells with cell centers in the left half of the box are labeled type 1, and the remainder are labeled type 2, and a mixed system where cell types are randomly assigned. We use FIRE minimization<sup>37</sup> to identify the nearest local energy minimum for 250 realizations in each of the two scenarios.

Fig. 4a shows the ratio between the energy of states with sorted initial conditions ( $E_s$ ) and mixed initial conditions ( $E_m$ ) in the case where type 1 and 2 cells have different shape parameters. At larger system sizes, there is a clear trend that the sorted states typically possess higher energies than the mixed states, so that the ratio rises above unity as the shape disparity  $\Delta$  increases. This indicates that there are no energetic forces driving the demixing in larger systems. We have also quantified the effective interfacial line tension (Fig. S4 and S5, ESI†)

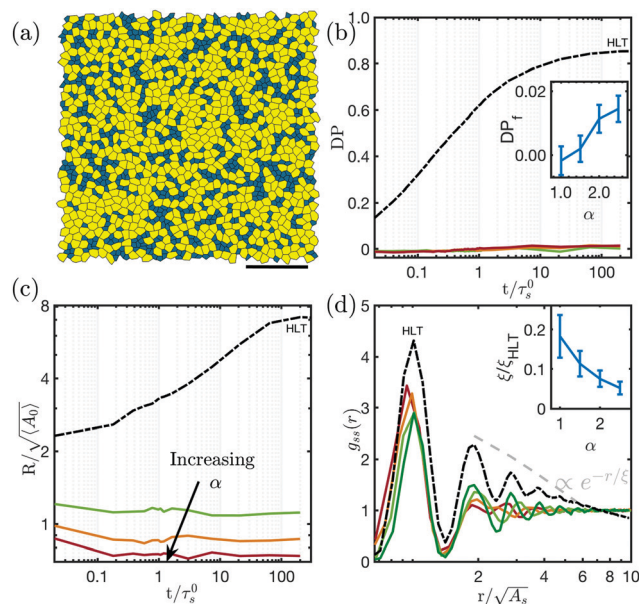


**Fig. 3** Area bidisperse fluid mixtures. (a) Snapshot of a  $s_0 = 3.85$ ,  $\alpha = 2.5$ ,  $N = 1600$  mixture. Scale bar denotes 10 units. Yellow is used for larger cells ( $A_0 = 1.43$ ) and blue for smaller ones ( $A_0 = 0.57$ ). (b)–(d) Various quantifications of demixing in area bidisperse mixtures (curves colored from green to red in increasing order of size disparity *i.e.*  $\alpha = 1.0, 1.5, 2.0, 2.5$ ) are compared to a mixture with an extra heterotypic line tension of value 0.1,  $s_0 = 3.97$  and  $A_0 = 1.0$  (black dashed curve). (b) Demixing parameter versus log(time). The final value ( $DP_f$ ) as a function of  $\alpha$  is shown in the inset. (c) Average cluster radius ( $R$ ) versus time. (d) Pair correlation function of small- $A_0$  cells ( $g_{ss}$ ) versus radial distance in units of the smallest lengthscale for  $t = 200\tau_s^0$ . The dashed grey line shows an exponential decay. The inset shows the decay lengthscale ( $\xi$ ) in terms of the maximum possible lengthscale ( $\xi_{HLT}$ ) with increasing disparity  $\Delta$ . Simulation details provided in Table S2 (ESI†).

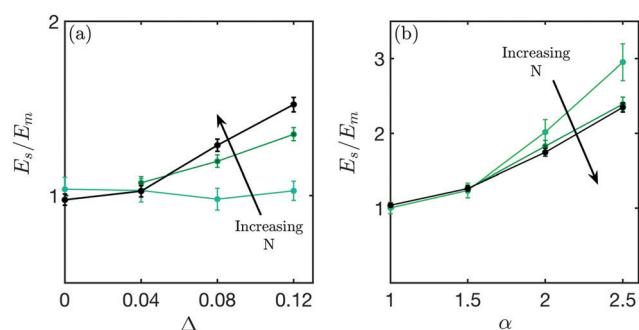


**Fig. 4** Minimal energy configurations. Systems with  $N = 100, 400$  and  $900$  cells (green to black) are energy minimized using the FIRE algorithm to get the total energy of the configurations—mixed ( $E_m$ ) and sorted ( $E_s$ ), for increasing value of disparity. (a) The ratio  $E_s/E_m$  is plotted versus  $\Delta$  for  $\langle s_{av} \rangle = 3.85$ ,  $K_a = 100$ . (b) The ratio  $E_s/E_m$  is plotted versus  $\alpha$  for  $s_0 = 3.85$  and  $K_a = 1$ . Simulation details provided in Table S3 (ESI†).

using a method developed previously by some of us.<sup>38</sup> We find that there is no emergent line tension in any of these mixtures, which is consistent with our energy calculations. In Fig. 4b, which shows the ratio of energies between sorted and mixed states for cells with area disparity, the trend is even clearer. Again, sorted states have

significantly higher energy compared to mixed states as the area disparity  $\alpha$  increases.

### Zero-temperature T1 energy barriers

Although the zero temperature energy calculations above help us understand the lack of macroscopic demixing in mixtures with no heterotypic interfacial tension, they do not explain the small-scale demixing seen, for example, in Fig. 2b. Since both cell types are subject to the same geometrical and topological constraints and rearrange *via* T1 transitions, we now turn to an energetic analysis of T1 transitions for the bidisperse system.

Specifically, we study the statistics of energy barriers in bidisperse systems, where there are nine types of T1 transitions possible. While we present data in the ESI† for symmetric cases where two of the cells are of type 1 and two of are type 2, we focus here on asymmetric systems where 3 of the cells are of one type and one is of another type. As illustrated by the 4-cell cluster diagrams in Fig. 5, such 3:1 arrangements naturally represent the cost of one cell type invading an interface.

Similarly to previous work,<sup>25,26</sup> we compute the T1 energy barrier height by measuring the global tissue energy as we force a single edge in our bidisperse simulation to shrink to zero length while minimizing the energy and allowing the other degrees of freedom to relax, as shown in Fig. 5a. The energy barrier  $E_b$  we report in Fig. 5b is the difference between the final energy  $E(l = 0)$  at the 4-fold vertex and the initial energy  $E_0$ , or  $E_b = E(l = 0) - E_0$ , averaged over 250 edges with the same topology in small simulated tissues with  $N = 80$  cells.

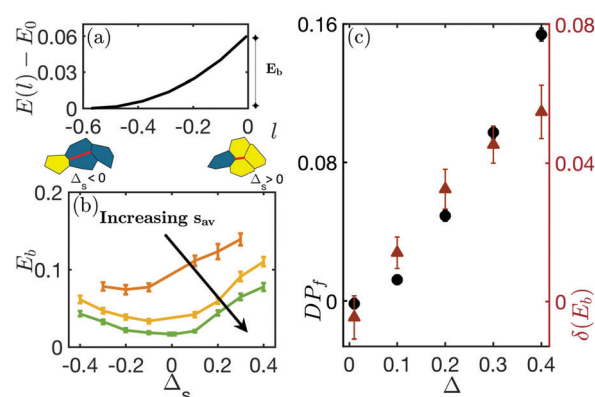


**Fig. 5** Differential energy barriers in shape bidisperse fluid mixtures. (a) Energy  $E(l)$  relative to  $E_0$  is plotted against T1 edgelenh  $l$  for a typical shape bi-disperse T1 pair ( $\Delta = 0.4$ ,  $s_{av} = 3.85$ ). (b) Energy Barrier  $E_b$  is plotted against signed disparity in shape  $\Delta_s$ . Positive and negative  $\Delta_s$  values imply stiffer cluster in yellow and floppier cluster in blue respectively, in the 4-cell diagrams show above. Each solid curve represents the barrier for a heterotypic cell to get out of the cluster for  $s_{av} = 3.79, 3.85, 3.88$  (from solid-like (orange) to liquid-like (green)). (c) correlation plot for  $s_{av} = 3.85$  between differential energy barriers on the right y-axis  $\delta(E_b)$  (in maroon triangles) and demixing relative to mixed scenario  $DP_f$  on the left y-axis (in black discs). Shape difference  $\Delta$  is plotted on x-axis. Simulation details provided in Table S4 (ESI†).

Fig. 5a illustrates a particular type of (3 : 1) T1 energy profile where a single cell with shape parameter  $s_0^1$  invades a 3-cell cluster formed by cells with  $s_0^{\text{cluster}}$ . We define a signed shape disparity  $\Delta_{\text{sign}} = s_0^1 - s_0^{\text{cluster}}$  to distinguish it from a T1 with cell types swapped. Negative  $\Delta_{\text{sign}}$  indicates that a more stiff cell is invading a cluster of floppy cells. We have checked that energy barriers are statistically identical for cells entering or exiting a cluster. Because cells are as likely to leave a cluster as to enter it, this suggests that clusters of a given cell type will not grow or shrink over long-time or length-scales.

Fig. 5b highlights that the energy barriers associated with these (3 : 1) transitions systematically increase as the magnitude of the shape dispersity  $\Delta_{\text{sign}}$  increases. In other words, it becomes energetically more difficult for a single cell to invade or leave a cluster of a different cell type as the shape dispersity between the two types increases. Perhaps more importantly, it also shows that these energy barriers are not symmetric around zero; there is a systematic difference between a stiffer cell invading a floppier cluster and *vice versa*, especially for lower values of  $s_{\text{av}}$  as the system approaches the jamming transition. Stiffer clusters tend to be more difficult to break up than floppier clusters. To characterize this effect, we define the energy barrier disparity between invading stiffer and floppier clusters as  $\delta E_b(\Delta) = E_b(\Delta) - E_b(-\Delta)$ .

To test whether this mechanism might be relevant for the micro-demixing we observed in our finite-temperature simulations, we directly compare the demixing parameter associated with the final, steady state in each simulation,  $\text{DP}_f$  to the energy barrier disparity  $\delta E_b$  as a function of shape dispersity  $\Delta$ , as shown in Fig. 5c. This plot shows a quite strong correlation between the two quantities, suggesting that this mechanism is a very likely driver of micro-demixing. To further test this idea, we have increased the temperature for the  $\Delta = 0.2$  mixtures and found DP to vanish at temperatures higher than the differential energy barrier, as shown in Fig. S3 (ESI<sup>†</sup>).

A similar analysis can be performed for area bidisperse mixtures as shown in Fig. S6 (ESI<sup>†</sup>). An important difference from the shape bidisperse case is that while there is a clear connection between cell shape and tissue rheology (stiffer cells have a smaller  $s_0$ ), there is no such connection between area and rheology. Moreover, there is very little evidence for micro-demixing, and so we expect the signal to be much weaker. Nevertheless, we can define a quantity  $\alpha_s = A_0^{\text{cluster}}/A_0^1$  that is less than unity if a larger cell is invading a cluster of smaller cells and greater than unity otherwise. Fig. S6b (ESI<sup>†</sup>) suggests that large-cell clusters are more difficult to invade than small-cell clusters, although the differential energy barrier is quite a bit smaller than for the case of shape bidispersity. In particular, the case where  $s_0 = 3.85$  is highlighted in Fig. S6c (ESI<sup>†</sup>) showing a correlation between demixing and  $\delta E_b$ , although the amplitude of both effects is quite small.

## Experimental results

To test our modeling against experiments, we first study monolayers of primary keratinocytes (Ctr) in the presence of high calcium, whose presence initiates intercellular junction

formation (see Fig. 6a). Under such conditions, the monolayer is confluent in the sense that there are essentially no gaps between cells. We also test whether the confluent monolayer is fluid-like by measuring the displacement of cells over the course of 24 hours. While some number of neighbor exchanges indeed take place, and while the integrated displacement of the cells is several times a typical cell length, we find that the mean square displacement of these cells is typically of the order of a single cell size (Fig. S10a, ESI<sup>†</sup>). This places some limitations on the scale of demixing that is expected, but we nevertheless see a level of micro-demixing that is comparable to what we observe in our simulations (Fig. S6e, ESI<sup>†</sup>).

Since the shape index is an important parameter in our theory, we measure this quantity for Ctr cells in the monolayer and obtain an average shape index of  $4.08 \pm 0.06$ . The full histogram is plotted in Fig. 6b. Confluent monolayers of primary keratinocytes but with E-cadherin knocked-out, or E-cad<sup>-/-</sup> cells, again in the presence of high calcium, are then studied to check for confluency (Fig. 6a) and fluidity (Fig. S10a, ESI<sup>†</sup>). We then measure an average shape index of  $4.38 \pm 0.14$  for the E-cad<sup>-/-</sup> cells (Fig. 6b). A *T*-test reveals that the difference in the two shape index histograms is statistically significant with a *P*-value of 0.0008. The difference in the shape index corresponds to  $\Delta = 0.31$ . Since we explore both differential adhesion and differential size, we also measure the areas of each cell type in the monolayer and found no statistically significant area difference. See Fig. S10(b) (ESI<sup>†</sup>). In other words, the monolayer mixture tests differential adhesion, as opposed to both differential adhesion and bidisperse areas.

Next, we study the monolayer of approximately a 50 : 50 Ctr/ E-cad<sup>-/-</sup> mixture in the presence of high calcium over the course of 24 hours. Again, a major complication in our comparison is that while both types of cells in the mixture exert active forces on their environment the typical displacements over this time frame are small. Nevertheless, after constructing a Voronoi tessellation for snapshots of the monolayer taken every hour, we measure the demixing parameter (DP) for each cell type, accounting for the fact that the mixture is not precisely a 50 : 50 mixture (see Fig. S10c, ESI<sup>†</sup>). In doing so, we measure number of neighbors for each cell type and subtract off the corresponding number fraction. Fig. 6e shows the DP parameter as a function of time for the E-cad<sup>-/-</sup> cells in the mixture. This parameter increases from zero (within one standard deviation) and appears to saturate after approximately 19 hours to around 0.15, albeit with some fluctuations. Such values of the DP parameter are consistent with our computational observations of micro-demixing in the differential adhesion case.

We argue that these results suggest the small-scale demixing is a consequence of large differences in differential adhesion. To rule out this being a consequence of the natural variability in adhesion even within one cell type, we also measure the demixing parameter in monolayers of just Ctr cells and of just E-cad<sup>-/-</sup> cells by staining half of the cells with one type of stain and the remaining half with a second type of stain (checking for an artificial “demixing” due to variability in these two monotypic monolayers). We find that the demixing parameter does



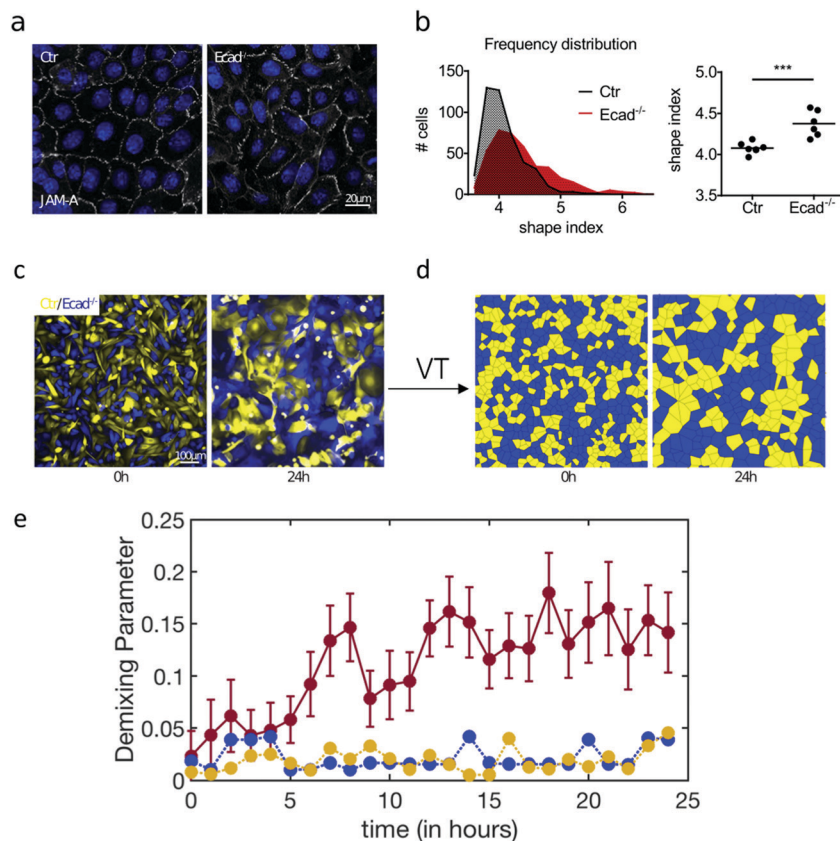


**Fig. 6** Micro-demixing observed in keratinocyte co-cultures. (a) Wild-type (Ctr) and E-cadherin knockout (E-cad<sup>-/-</sup>) cell monolayer mixtures with nuclei labelled using immunofluorescence. (b) Histograms of cell shapes for Ctr and E-cad<sup>-/-</sup> cells are compared across seven and six different isolates respectively, *i.e.* seven different mice. There is a clear difference in the shape index ( $A = 0.31$ ) of both cell-types, with shape indices being  $4.08 \pm 0.06$  for Ctr cells and  $4.38 \pm 0.14$  for Ecad<sup>-/-</sup> cells. (c) Both cell-types, Ctr in yellow and E-cad<sup>-/-</sup> in blue, start off initially mixed as shown the 0 h (zero hours) snapshot. The co-culture evolves into a micro-segregated mixture, as shown in a 24 h snapshot. (d) Voronoi tessellations (VT) of the same snapshots. (e) Solid maroon curve represents the time evolution of demixing parameter for the E-cad<sup>-/-</sup> cell-type in the mixture as a function of time and averaged over five different isolates. This result is compared against a control of demixing curves for some initially well-mixed regions of monolayers of either all Ctr cells or all E-cad<sup>-/-</sup> cells but with half the cells stained differently than the other half. Well-mixed regions of the control cells are shown in yellow, while the well-mixed regions of the E-cad<sup>-/-</sup> cell-type is shown in blue.

not increase over time on average for either the Ctr cells or the E-cad<sup>-/-</sup> cells when looking at initially well-mixed regions (Fig. 6e) or the entire monolayer (Fig. S11a, ESI†). In addition to the DP, we also compute the pair-correlation function for the experimental system and find that while it contains less structure than the simulations, it also exhibits a correlation length over several cell diameters (see Fig. S11b and c, ESI†).

While the qualitative and semi-quantitative comparison between the degrees of micro-demixing observed in experiments and vertex model simulations is promising, we must also acknowledge that there are several differences between the two settings. Taking into account such differences and determining how the micro-demixing is potentially affected is a future avenue for investigation. For instance, our computations so far focus on 50 : 50 mixtures and do not take into account the potentially persistent motion of cells. Another difference is the apparent timescale over which the micro-demixing occurs from various initial conditions: in the experiments the demixing seems to occur during a time in which the cells move not much more than a typical cell size; in contrast our simulations

require many  $\tau_x$  to reach comparable levels of demixing from a random initial configuration. Additionally, while we expect the differential energy barriers to remain at least for some range of persistence, the value of the DP parameter will depend on that just as the steady state value of the DP parameter depends on temperature in our over-damped Brownian simulations. Further differences may include the effect of differential motility, differential mechanical stiffnesses of the cells, and differential cell division and death (which can itself affect the diffusivity of cells<sup>39</sup>). Therefore, to more rigorously test the computations against the experiments, future experimental work with detailed cell tracking within the monolayer and the prevention of cell birth with the introduction of mitomycin, as well as additional computational work, needs to be implemented.

## Discussion

Using Brownian vertex model simulations, we show that two-dimensional mixtures, bidisperse in preferred shape and in



preferred area, have robust fluid-phase mixing at large scales in the absence of an explicit heterotypic line tension distinguishing between the two cell types. Energy minimization at zero temperature further supports this finding: mixed systems have lower energy than sorted ones, so that bidispersity is not sufficient to energetically stabilize an interface between the two fluids. For shape bidisperse mixtures, we find that, in spite of having solid-like cells making up half the mixture, the mixtures are still able to fluidize in some parameter regimes of the vertex model. Furthermore, although this large scale mixing occurs, we find persistent and equally robust micro-demixing in shape bidisperse mixtures, where clustering of the same cell type over sub-system-spanning lengthscales is observed.

To understand micro-demixing in shape bidisperse mixtures, we establish a correlation between micro-demixing and zero-temperature differential energy barriers for neighbor exchanges (T1 transitions) between four cells at the heterotypic boundaries. Specifically, we find that the energy barriers for a fluid cell type to “invade” a cluster of stiff cells is typically higher than for a stiff cell to “invade” a cluster of fluid cells. This difference in energy barriers creates a bias towards the small-scale clustering of stiffer cells. For area bidisperse systems, the differential energy barriers for neighbor exchanges are smaller than for the shape bidisperse case, and we find a negligible amount of micro-demixing. Our differential energy barrier calculations at zero temperature also yields a prediction for the temperature above which the micro-demixing does not occur – a prediction that has indeed been verified in our simulations.

The computational observation of robust mixing on large scales for both types of mixtures may be surprising, given that the shape-based interaction distinguishes between the two cell types just as changing the strength of the distance-dependent interaction between two particles of different types in thermal Lennard-Jones mixtures. In the particulate case, there is either large-scale demixing or no demixing (depending on the miscibility), while in the cellular case, there can be micro-demixing. This suggests that vertex models may be more relevant for characterizing cell sorting in dense cellular mixtures than other coarse-grained modeling approaches.

What about comparisons with athermal particle systems? Athermal two-dimensional bidisperse particulate mixtures of different size discs with purely repulsive forces, such as models for granular particles with no (or little) friction, are not expected to sort at small size disparities.<sup>40</sup> Only as the size dispersity increases does sorting occur due to entropic depletion forces.<sup>41</sup> Entropic depletion forces do not apply to a confluent tessellation in which the packing fraction is fixed at unity, though may to some extent apply to Voronoi models. Depletion forces also drive demixing in vertical vibrated shape bidisperse mixtures of rods and spheres.<sup>42</sup> Interestingly, size bidisperse mixtures of active particles can sort in the absence of any attractive forces.<sup>43</sup> The sorting here is due to an asymmetry in the energy barrier between one smaller particle passing through two larger particles as compared to one larger particle passing through two smaller ones. Given the above analogy, a vertex model fluid mixture perhaps has more in common with an active, disordered binary

packing than with a thermal fluid mixture with differential adhesion.

How different is the vertex model examined here applied to cells in comparison to the vertex models applied to foams? The robust mixing observed in area bidisperse systems at zero temperature is indeed counter-intuitive when compared with area bidisperse foams in ordered hexagonal states.<sup>30</sup> In this case, the system demixes at zero temperature given an additional perturbative energetic cost to an interface between cells of slightly different areas. Only for large applied shear strains do area bidisperse foams mix.<sup>31</sup> Understanding differences between foam and vertex models is therefore an interesting area for future study. Foam models lack the  $P^2$  contribution to the energy functional (eqn (1)) and this restricts the fluid-like phase space accessible to such models, perhaps contributing to differences between them.

To determine whether or not our micro-demixing prediction is directly relevant for biology, we conduct experiments with cellular monolayers consisting of both wild-type keratinocytes and E-cadherin-knock-out keratinocytes. Such mixtures allow us to study differential adhesion and its effect on cell sorting in the absence of heterotypic tensions. We find evidence for micro-demixing with a saturated demixing parameter that agrees with our prediction to within one standard deviation of the experimental value. Moreover, we do not observe large-scale demixing over the time scale of the experiment. Over longer time scales, the monolayers gradually become multi-layered, an effect we have yet to incorporate into our computational modeling of confluent cellular mixtures. In addition to cell persistence, differential motility, and cell birth/death, we also have yet to explore the effects of small lapses in confluency, which could arise given the lack of E-cadherin in the modified cell type. Such exploration will allow for even more rigorous quantitative comparison between the modeling and the experiments.

Our computational and experimental results bring an understanding to earlier work demonstrating that sorting at embryonic boundaries requires high heterotypic interfacial tension.<sup>33</sup> Given our T1 energy barrier analysis encoding both the topological and geometrical constraints of confluent packings, we now understand why these mixtures robustly mix. This robustness suggests that despite some difference in shape and size, progenitor cells can readily mix throughout the embryo. To demix (or sort), progenitor cells have developed biochemical means of recognizing whether neighboring cells are of the same type or a different types. And while a small amount of heterotypic line tension can generate stable interfaces<sup>32</sup> in the absence of fluctuations, correlated fluctuations may be able to overcome such barriers. Our analysis gives a new way to understand bulk behavior based on cellular rearrangements in such confluent mixtures. In other words, based on the analysis of T1 energy barriers between different cell types, experimentalists can predict whether or not different cell types will mix or not mix in the bulk.

Finally, the micro-demixing effect observed both in our computations and in our experiments could be utilized in biology to create more subtle patterning. For instance, when

randomly tagging a tessellation half with one cell type (and half with another cell type), one of the cell types percolates through the system.<sup>44</sup> However, if there is now some spatial correlation in the tagging introduced even at the small scale, such that the tagging of one cell type is positively correlated with tagging a neighboring cell of the same type, then the percolation transition point can be altered, transitioning from a tenuous spanning structure to one that is more robust and more able to respond to changes in the environment.

## Methods and materials

### Simulation details

We simulate a vertex model where the degrees of freedom evolve according to over-damped Brownian dynamics.<sup>45</sup> Specifically, each vertex  $i$  located at coordinate  $\mathbf{r}$  experiences a Brownian force  $\mathbf{F}^B$  with  $\mathbf{F}_i^B = \xi_i$ , where  $\xi_i$  is white noise with zero mean and  $\langle \xi_{\gamma i}(t) \xi_{\lambda k}(t') \rangle = 2T \delta_{\gamma\lambda} \delta_{ik} \delta(t - t')$  with  $\gamma$  and  $\lambda$  denoting spatial components and in units of  $k_B$  equal to unity. In epithelial layers, we expect that fluctuations are driven by active cytoskeletal components, and hence the  $T$  is an effective temperature that represents the magnitude of this activity (ref. 46). The equation of motion for a single vertex, therefore, takes the form

$$\dot{\mathbf{r}}_i = \mu \mathbf{F}_i + \mu \mathbf{F}_i^B, \quad (5)$$

with  $\mathbf{F}_i = -\nabla_i E$ , where  $E$  is the total energy as defined in the Model section. The force  $\mathbf{F}_i$  is a non-local effective mechanical force experienced by the  $i$ th vertex of the  $j$ th cell and hence represents the cell–cell interactions. In the absence of mechanical interactions, an isolated cell performs a random walk with a long time effective diffusion rate of  $T/\mu$ . Unless otherwise specified,  $\mu = 1$ . Finally, the Euler–Murayama integration method is used to update a discretized version of the equations (one for each vertex). One simulation unit time is referred to as  $\tau$ . For a system with no dispersity, a cell with a shape parameter  $s_0$  of 3.85, typically requires  $1000\tau$  to move its own length, *i.e.*  $\tau_s^0 = 1000\tau$ . We typically simulate up to times several hundred times greater than  $\tau_s^0$ . We also note that other models with directed cell motility are possible, including an active vertex model<sup>47</sup> and the SPV model where cells are self-propelled due to an active force with persistence.<sup>24,26</sup>

In vertex models, one needs to take care of cellular rearrangements explicitly.<sup>22,26</sup> In the absence of cell division or death, such rearrangements correspond to T1 transitions in which one edge shrinks to zero length and two new cells are connected *via* a new growing edge. In simulations, if an edge length falls below some threshold length  $l_c$ , then we rotate the edge by  $\pi/2$  and reconnect the topology of the surrounding cells to generate a local neighbor-exchange. Unless otherwise specified,  $l_c$  is set to 0.04. The noise is controlled by temperature ( $T$ ) which is set to 0.01.

Past work has demonstrated that the mechanical properties of vertex models depend sensitively on the shape parameter  $s_0$  and temperature  $T$ . Specifically, these models exhibit rigidity<sup>25</sup>

or glass<sup>48</sup> transitions where the system transitions from more solid-like to more fluid-like. At  $T = 0$ , the 2D vertex model exhibits a rigidity transition as a function of cell shape parameterized by  $s_0$ . Above a critical value of target shape index  $s_0^* \sim 3.81$ , cells are able to move past each other with very small energy cost and below which they cannot. To understand this transition, one analyzes the energetics of how cells move past each other *via* T1 transitions. A minimal four cell calculation with fixed unit area hexagonal cells revealed that if the two cells that would no longer share an edge after the edge swap formed regular pentagons, then the energy barrier for the formation of a four-vertex vanishes, suggesting that pentagon shape formation is a geometrically compatible transition pathway for three-fold coordinated lattices. Interestingly, the shape parameter for a regular pentagon is  $s_0 = 2\sqrt{5}(5 - 2\sqrt{5})^{1/4} \approx 3.812 \approx s_0^*$ . In the presence of activity or temperature, vestiges of this zero-temperature rigidity transition have been found in a glassy transition between fluid-like and more solid-like behavior in an active Self-Propelled Voronoi (SPV) model<sup>26</sup> and a Brownian Voronoi model.<sup>48</sup>

Given the complex phase behavior of such vertex models, we want to ensure that the mixtures are fluid-like. To do so, we first measure the Mean-Squared Displacement (MSD). To account for global tissue motion possible in these types of models,<sup>49</sup> we define the displacement of each cell in a time window  $t$ ,  $\mathbf{x}(t)$ , as the distance the cell traveled in time  $t$  minus the total displacement of the entire system of cells over that same time interval. Then the MSD is defined as

$$\text{MSD}(\Delta t) \equiv \langle (\mathbf{x}(t + \Delta t) - \mathbf{x}(t))^2 \rangle, \quad (6)$$

where  $\langle \cdot \rangle$  denotes an average over all cells in the tissue and all times  $t$ . The self-diffusivity  $D_s$ , is defined by assuming the long-time behavior of the system is diffusive,

$$D_s = \lim_{t \rightarrow \infty} \frac{\text{MSD}(t)}{4t}. \quad (7)$$

To understand whether cells are being constrained by their neighbors, we compare  $D_s$  to the bare, or non-interacting, diffusion constant  $D_0$ . For a non-interacting Brownian particle at temperature  $T$  with mobility  $\mu$ , the Fluctuation–Dissipation theorem states that  $D_0 = \mu k_B T$ , where  $k_B$  is Boltzmann constant. We set  $\mu k_B$  to unity. The effective diffusivity is given by

$$D_{\text{eff}} = \frac{D_s}{D_0}. \quad (8)$$

Systems with small  $D_{\text{eff}}$  are more solid-like, while systems with large  $D_{\text{eff}}$  are more fluid-like. In practice, we use a threshold of 0.01 to distinguish between these different behaviors, in line with previous work.<sup>26</sup>

Self-diffusivity time  $\tau_s$  is defined as the time taken by a cell to move its own length. For a 2D system, one can use eqn (7) to compute  $\tau_s = 1/4D_s$ . Dispersity in the system can affect this average motion. Hence we convey time in units of  $\tau_s^0$  which we define as the self-diffusivity of cell, with  $s_0$  of 3.85, in absence of any dispersity. To study micro-demixing, we run simulations

that are  $200\tau_s^0$  long *i.e.* long enough for cells to explore the entire system multiple times.

## Experimental details

### Isolation and culture of primary keratinocytes

Primary keratinocytes isolated from newborn mice were cultured in DMEM/HAM's F12 (FAD) medium with low  $\text{Ca}^{2+}$  (50  $\mu\text{M}$ ) (Biochrom) supplemented with 10% FCS (chelated), penicillin (100 U  $\text{ml}^{-1}$ ), streptomycin (100  $\mu\text{g ml}^{-1}$ , Biochrom A2212), adenine ( $1.8 \times 10^4$  M, SIGMA A3159), L-glutamine (2 mM, Biochrom K0282), hydrocortisone (0.5  $\mu\text{g ml}^{-1}$ , Sigma H4001), EGF (10 ng  $\text{ml}^{-1}$ , Sigma E9644), cholera enterotoxin ( $10^{10}$  M, Sigma C-8052), insulin (5  $\mu\text{g ml}^{-1}$ , Sigma I1882), and ascorbic acid (0.05 mg  $\text{ml}^{-1}$ , Sigma A4034). For keratinocyte isolation newborn mice were sacrificed by decapitation and incubated in 50% Bataisodona/PBS for 30 minutes at 4 °C, 1 minute PBS, 1 minute 70% EtOH, 1 minute PBS and 1 minute antibiotic/antimycotic solution. Tail and legs were removed and complete skin incubated in 2 ml Dispase (5 mg  $\text{ml}^{-1}$ )/FAD solution. After incubation over night at 4°C, skin was transferred onto 500  $\mu\text{l}$  FAD medium on a 6 cm dish and epidermis was separated from the dermis as a sheet. Epidermis was transferred dermal side down onto 500  $\mu\text{l}$  of TrypLE (ThermoFisher Scientific) and incubated for 20 minutes at RT. Keratinocytes were washed out of the epidermal sheet using 3 ml of 10%FCS/PBS. After centrifugation keratinocytes were resuspended in FAD medium and seeded onto Collagen type-1 (0.04 mg  $\text{ml}^{-1}$ ) (Biochrom, L7213) coated cell culture plates. Primary murine keratinocytes were kept at 32°C and 5%  $\text{CO}_2$ . To induce classical cadherin dependent junction formation, cells were switched to high  $\text{Ca}^{2+}$  medium (1.5–1.8 mM). Cultured cells were regularly monitored for mycoplasma contamination and discarded in case of positive results. E-cadherin<sup>−/−</sup> keratinocytes were isolated from E-cadherin epidermal knockout mice as described previously.<sup>35</sup>

### Keratinocyte labeling and demixing assay

Keratinocytes were resuspended according to 500 000 cells per ml in 1 ml dyeing solution (medium with 10  $\mu\text{M}$  CellTracker Green or CellTracker™ Orange (ThermoFisher #C7025 or #C34551 respectively, stock 10 mM in DMSO)). Cells were incubated for 20 minutes at 32 °C and pelleted at 850 rpm for 5 minutes. Cells were resuspended in 1 ml medium and incubated for another 30 minutes at 32 °C. Eventually, cells were pelleted again and resuspended in 1 ml and green and orange cells of equal numbers were mixed and plated in low  $\text{Ca}^{2+}$  FAD medium. Cell numbers were chosen to achieve confluency immediately after attachment and spreading. Twenty-four hours after plating medium was changed either low or high  $\text{Ca}^{2+}$  FAD medium to induced cell-cell junction formation and demixing. Prior to live cell imaging, cells were incubated in FAD medium containing Hoechst dye to label nuclei for 1 hour. During live cell imaging cells were kept under controlled temperature (37 °C) and  $\text{CO}_2$  (5%) and imaged every hour.

### Immunofluorescence of keratinocytes *in vitro* (cell shape)

For immunofluorescence staining of keratinocytes, cells were seeded on collagen coated glass cover slips in a 24 well plate and switched to high  $\text{Ca}^{2+}$  medium at confluency for 2 hours. Cells were fixed using 4%PFA for 10 minutes at RT, washed three times for 5 minutes using PBS, permeabilized using 0.5%TritonX100/PBS and blocked using 5%NGS/1%BSA/PBS for 1 hour at room temperature. Primary antibodies were diluted as indicated in the antibody section in Background Reducing Antibody Diluent Solution (DAKO). Cover slips were placed growth surface down onto a 50  $\mu\text{l}$  drop of staining solution on parafilm in a humidified chamber and incubated over night at 4 °C. Cover slips were transferred back into the 24 well plate and washed with PBS three times for 10 minutes. Secondary antibodies and DAPI (4',6-diamidin-2-phenylindol, Sigma) were diluted 1:500 in PBS and cover slips were incubated for 1 hour at RT. Secondary antibodies were washed off *via* three wash steps using PBS for 10 minutes. Cover slips were mounted using Gelvatol (Calbiochem).

### Antibodies and inhibitors

Primary antibodies used in this study: rat monoclonal against ZO-1 (hybridoma supernatant,<sup>50</sup> clone R26.4C); rat monoclonal against JAM-A (1:300, clone H<sub>2</sub>O<sub>2</sub>-106-7-4, kind gift from Sandra Iden). Secondary antibodies were species-specific antibodies conjugated with either AlexaFluor 488, 594 or 647, used at a dilution of 1:500 for immunofluorescence (Molecular Probes, Life Technologies).

### Microscopy

Confocal images were obtained with a Leica TCS SP8, equipped with a white light laser and gateable hybrid detectors (HyDs). Objectives used with this microscope: PlanApo 63 $\times$ , 1.4 NA. Epifluorescence images were obtained with a Leica DMI6000. Objectives used with this microscope: PlanApo 63 $\times$ , 1.4 NA; PlanApo 20 $\times$ , 0.75 NA.

### Image processing and analysis

Quantification of cell shapes: Keratinocyte cell shapes were analyzed 2 hours after  $\text{Ca}^{2+}$  switch and induction of cell-cell junction formation. Cell-cell boundaries were labeled by staining for one of two early cell-cell junction markers ZO-1 or JAM-A. Images were analyzed using Fiji.<sup>51</sup> Cell-cell boundaries were delineated manually using the polygon tool and perimeter and area were measured to calculate the shape index as described above.

Keratinocyte demixing: Leica Imaging Files (LIF) were analyzed using cell profiler 3.1.9.<sup>52</sup> Nuclei of cells were identified and nuclei areas were used to measure green fluorescence to discriminate between green and red cells.

## Code availability

The codes are programmed using open source cellGPU code available at <https://github.com/sussmanLab/cellGPU><https://github.com/sussmanLab/cellGPU>.

## Data availability

The data that support the findings of this study are available from the corresponding authors upon reasonable request.

## Author contributions

All authors conceived the study; P. S. conducted the simulations; M. R. and A. M. conducted experiments; P. S., D. M. S., A. F. M. and M. R. contributed to the analysis; all authors interpreted the results and wrote the paper.

## Conflicts of interest

The authors declare no competing financial or non-financial interests.

## Acknowledgements

We would like to thank Matthias Merkel for useful discussions. We greatly acknowledge Peter Zentis and the CECAD Imaging Facility (University of Cologne) for help with image analysis and quantification. This work was supported by NSF-POLS-1607416 (MCM, MLM, JMS) NSF-DMR-1352184 (MLM), Simons Foundation-454947 (MLM), Simons Foundation-342345 (MCM), and the Deutsche Forschungsgemeinschaft (DFG, German Research Foundation) under Germany's Excellence Strategy – CECAD, EXC 2030 – 390661388, Project-ID 73111208 – SFB 829, and project ID NI1234/6-2 – SPP1782 (CN). SP, DMS, MLM, and JMS also acknowledge support of the Syracuse University Soft and Living Matter Program and BioInspired Syracuse.

## References

- 1 S. A. Safran, Statistical thermodynamics of soft surfaces, *Surf. Sci.*, 2002, **500**, 127–146.
- 2 D. Frenkel and A. A. Lousi, Phase separation in binary hard-core mixtures: An exact result, *Phys. Rev. Lett.*, 1992, **68**, 3363.
- 3 J. W. Cahn and J. E. Hillard, Free energy of a nonuniform system. i. interfacial free energy, *J. Chem. Phys.*, 1958, **28**, 258.
- 4 J. S. Rowlinson and F. L. Swinton. *Liquids and Liquids Mixtures*, Elsevier, 3rd edn, 1982.
- 5 M. Feric, N. Vaidya, T. S. Harmon, D. M. Mitrea, L. Zhu and T. M. Richardson, *et al.*, Coexisting Liquid Phases Underlie Nucleolar Subcompartments, *Cell*, 2016, **165**, 1686–1697.
- 6 M. S. Steinberg, Reconstruction of tissues by dissociated cells. Some morphogenetic tissue movements and the sorting out of embryonic cells may have a common explanation, *Science*, 1963, **141**, 401–408.
- 7 A. K. Harris, Is cell sorting caused by differences in the work of intercellular adhesion? a critique of the steinberg hypothesis, *J. Theor. Biol.*, 1976, **61**, 267–285.
- 8 G. W. Brodland, The Differential Interfacial Tension Hypothesis (DITH): A Comprehensive Theory for the Self-Rearrangement of Embryonic Cells and Tissues. AMSE, *J. Biomech. Eng.*, 2002, **124**, 189–197.
- 9 S. Yamada and W. James, Nelson. Localized zones of Rho and Rac activities drive initiation and expansion of epithelial cell–cell adhesion, *J. Cell Biol.*, 2007, **178**, 517.
- 10 Jean Léon Maître, Hélène Berthoumieux, Simon Frederik Gabriel Krens, Guillaume Salbreux, Frank Jülicher and Ewa Paluch, *et al.*, Adhesion functions in cell sorting by mechanically coupling the cortices of adhering cells, *Science*, 2012, **338**, 253–256.
- 11 M. Lisa Manning, Ramsey A. Foty, Malcolm S. Steinberg and E.-M. Schoetz, Coaction of intercellular adhesion and cortical tension specifies tissue surface tension, *Proc. Natl. Acad. Sci. U. S. A.*, 2010, **107**, 12517–12522.
- 12 J. D. Amack and M. L. Manning, Knowing the boundaries: Extending the differential adhesion hypothesis in embryonic cell sorting, *Science*, 2012, **338**, 212.
- 13 A. F. Mertz, S. Banerjee, Y. Che, G. K. German, Y. Xu and C. Hyland, *et al.*, Scaling of traction forces with the size of cohesive cell colonies, *Phys. Rev. Lett.*, 2012, **108**, 198101.
- 14 J. Heasman, D. Ginsberg, B. Geiger, K. Goldstone, T. Pratt and C. Yoshida-Noro, *et al.*, A functional test for maternally inherited cadherin in *Xenopus* shows its importance in cell adhesion at the blastula stage, *Develop*, 1993, **120**, 49.
- 15 W. Song, C. K. Tung, Y. C. Lu, Y. Pardo, M. Wu and M. Das, *et al.*, Dynamic self-organization of microwell-aggregated cellular mixtures, *Soft Matter*, 2016, **12**, 5739.
- 16 H. Ninomiya, R. David, E. W. Damm, F. Fagotto, C. M. Niessen and R. Winklbauer, Cadherin-dependent differential cell adhesion in *Xenopus* causes cell sorting in vitro but not in the embryo, *J. Cell Sci.*, 2012, **125**, 1877.
- 17 S. Pawlizak, A. W. Fritsch, S. Grosser, D. Ahrens, T. Thalheim and S. Riedel, *et al.*, Testing the differential adhesion hypothesis across the epithelial–mesenchymal transition, *New J. Phys.*, 2015, **17**, 091001.
- 18 J. J. Dong and S. Klumpp, Simulation of colony pattern formation under differential adhesion and cell proliferation, *Soft Matter*, 2018, **14**, 1908.
- 19 Katharina P. Landsberg, Reza Farhadifar, Jonas Ranft, Daiki Umetsu, Thomas J. Widmann and T. Bittig, *et al.*, Increased Cell Bond Tension Governs Cell Sorting at the *Drosophila* Anteroposterior Compartment Boundary, *Curr. Biol.*, 2009, **19**, 1950.
- 20 O. Cochet-Escartin, T. T. Locke, W. H. Shi, R. E. Steele and E. M. S. Collins, Physical Mechanisms Driving Cell Sorting in *Hydra*, *Biophys. J.*, 2017, **113**, 2827.
- 21 T. Nagai and H. Honda, A dynamic cell model for the formation of epithelial tissues, *Philos. Mag. B*, 2001, **81**, 699–719.
- 22 R. Farhadifar, B. Röper, J. C. Aigouy, S. Eaton and F. Jülicher, The Influence of Cell Mechanics, Cell–Cell Interactions, and Proliferation on Epithelial Packing, *Curr. Biol.*, 2007, **24**, 2095–2104.
- 23 D. B. Staple, R. Farhadifar, J. C. Röper, B. Aigouy, S. Eaton and F. Jülicher, Mechanics and remodelling of cell packings in epithelia, *Eur. Phys. J. E: Soft Matter Biol. Phys.*, 2010, **33**, 117–127.



- 24 D. L. Barton, S. Henkes, C. J. Weijer and R. Sknepnek, Active vertex model for cell-resolution description of epithelial tissue mechanics, *PLoS Comput. Biol.*, 2017, **13**, e1005569.
- 25 D. Bi, J. H. Lopez, J. M. Schwarz and M. L. Manning, A density-independent rigidity transition in biological tissues, *Nat. Phys.*, 2015, **11**, 1074–1079.
- 26 D. Bi, X. Yang, M. C. Marchetti and M. L. Manning, Motility-driven glass and jamming transitions in biological tissues, *Phys. Rev. X*, 2016, **6**, 021011.
- 27 Jin Ah Park, *et al.*, Unjamming and cell shape in the asthmatic airway epithelium, *Nat. Mater.*, 2015, **14**, 1040–1048.
- 28 D. M. Sussman and M. Merkel, No unjamming transition in a voronoi model of biological tissue, *Soft Matter*, 2018, **14**, 3397–3403.
- 29 M. Moshe, M. Bowick and M. C. Marchetti, Geometric frustration and solid–solid transitions in model 2D tissue, *Phys. Rev. Lett.*, 2018, **120**, 268105.
- 30 F. Graner, *Two-Dimensional Fluid Foams at Equilibrium. in Morphology of Condensed Matter & Physics and Geometry of Spatially Complex Systems*, Springer-Verlag, Berlin, 2002.
- 31 S. J. Cox, The mixing of bubbles in two-dimensional bidisperse foams under extensional shear, *J. Non-Newtonian Fluid Mech.*, 2006, **137**, 39–45.
- 32 Daniel M. Sussman, J. M. Schwarz, M. Cristina Marchetti and M. Lisa Manning, Soft yet Sharp Interfaces in a Vertex Model of Confluent Tissue, *Phys. Rev. Lett.*, 2018, **120**, 058001.
- 33 L. Canty, E. Zarour, L. Kashkooli, P. François and F. Fagotto, Sorting at embryonic boundaries requires high heterotypic interfacial tension, *Nat. Commun.*, 2017, **8**, 157.
- 34 C. Neissen, D. Leckband and A. S. Yap, Tissue organization of cadherin adhesion molecules: dynamic molecular and cellular mechanisms of morphogenetic regulation, *Physiol. Rev.*, 2011, **91**, 691–731.
- 35 M. Rübsam, *et al.*, E-cadherin integrates mechanotransduction and EGFR signaling to control junctional tissue polarization and tight junction positioning, *Nat. Commun.*, 2017, **8**, 1–15.
- 36 F. Graner and J. A. Glazier, Simulation of biological cell sorting using a two-dimensional extended Potts model, *Phys. Rev. Lett.*, 1992, **69**, 213–216.
- 37 E. Bitzek, P. Koskinen, F. Gähler, M. Moseler and P. Gumbsch, Structural relaxation made simple, *Phys. Rev. Lett.*, 2006, **97**, 170201.
- 38 Xingbo Yang, Dapeng Bi, Michael Czajkowski, Matthias Merkel, M. Lisa Manning and M. Cristina Marchetti, Correlating cell shape and cellular stress in motile confluent tissues, *Proc. Natl. Acad. Sci. U. S. A.*, 2017, **114**, 12663–12668.
- 39 M. Czajkowski, D. M. Sussman, M. C. Marchetti and M. L. Manning, Glassy dynamics of models of confluent tissue with mitosis and apoptosis, *Soft Matter*, 2019, **15**, 9133–9149.
- 40 E. López-Sánchez, C. D. Estrada-Álvarez, G. Pérez-Ángel, J. M. Méndez-Alcaraz, P. González-Mozuelos and R. Castañeda-Priego, Demixing transition, structure, and depletion forces in binary mixtures of hard-spheres: The role of bridge functions, *J. Chem. Phys.*, 2013, **139**, 104908.
- 41 P. Melby, A. Prevost, D. A. Egolf and J. S. Urbach, Depletion force in a bidisperse granular layer, *Phys. Rev. E: Stat., Nonlinear, Soft Matter Phys.*, 2007, **76**, 051307.
- 42 G. M. Rodríguez-Liñán, Y. Nahmad-Molinari and G. Pérez-Ángel, Clustering-induced attraction in granular mixtures of rods and spheres, *PLoS One*, 2016, **11**, e0156153.
- 43 X. Yang, M. L. Manning and M. C. Marchetti, Aggregation and segregation of confined active particles, *Soft Matter*, 2014, **10**, 6477–6484.
- 44 B. Bollobás and O. Riordan, The critical probability for random voronoi percolation in the plane is 1/2, *Prob. Th. Rel. Fields*, 2006, **136**, 417–468.
- 45 D. M. Sussman, cellGPU: Massively parallel simulations of dynamic vertex models, *Comput. Phys. Commun.*, 2017, **219**, 400–406.
- 46 S. J. Gunst and J. J. Fredberg, The first three minutes: smooth muscle contraction, cytoskeletal events, and soft glasses, *J. Appl. Physiol.*, 2003, **95**, 413–425.
- 47 M. Czajkowski, D. Bi, M. L. Manning and M. C. Marchetti, Hydrodynamics of shape-driven rigidity transitions in motile tissues, *Soft Matter*, 2018, **14**, 5628–5642.
- 48 Daniel M. Sussman, M. Paoluzzi, M. Cristina Marchetti and M. Lisa Manning, Anomalous glassy dynamics in simple models of dense biological tissue, *Europhys. Lett.*, 2018, **121**, 36001.
- 49 F. Giavazzi, C. Malinverno, G. Scita and R. Cerbino, Tracking-Free Determination of Single-Cell Displacements and Division Rates in Confluent Monolayers, *Front. Phys.*, 2018, **6**, 120.
- 50 B. R. Stevenson, *et al.*, Identification of ZO-1: A high molecular weight polypeptide associated with the tight junction (zonula occludens) in a variety of epithelia, *J. Cell Biol.*, 1986, **103**, 755–766.
- 51 J. Schindelin, *et al.*, Fiji: an open source platform for biological-image analysis, *Nat. Methods*, 2012, **9**, 676–682.
- 52 C. McQuin, *et al.*, CellProfiler 3.0: Next-generation image processing for biology, *PLoS Biol.*, 2018, 1–17.